Molecular Imaging • Vol. 4, No. 2, April 2005, pp. 117–127

Development of a Single Detector Ring Micro Crystal Element Scanner: QuickPET II

Robert S. Miyaoka, Marie L. Janes, Kisung Lee, Byungki Park, Paul E. Kinahan, and Tom K. Lewellen

University of Washington

Abstract

This article describes a single ring version of the micro crystal element scanner (MiCES) and investigation of its spatial resolution imaging characteristics for mouse positron emission tomography (PET) imaging. This single ring version of the MiCES system, referred to as QuickPET II, consists of 18 MiCE detector modules mounted as a single ring in a vertical gantry. The system has a 5.76-cm transverse field of view and a 1.98-cm axial field of view. In addition to the scanner and data acquisition system, we have developed an iterative reconstruction that includes a model of the system's detector response function. Evaluation images of line sources and mice have been acquired. Using filtered backprojection, the resolution for a reconstructed line source has been measured at 1.2 mm full width at half maximum. F-18-2-fluoro-2-deoxyglucose mouse PET images are provided. The result shows that QuickPET II has the imaging characteristics to support high-resolution, static mouse PET studies using 18-F labeled compounds. *Mol Imaging* (2005) **4,** 117–127.

Keywords: Positron emission tomography, PET, high resolution, mouse imaging.

Introduction

The desire for noninvasive, high-resolution, in vivo imaging technology is being driven by the burgeoning field of molecular imaging, where the mouse is the main laboratory animal. It is estimated that over 90% of all mammals used in research in the year 2000 were mice [1]. The use of murine models is driven by three factors: advances in molecular genomics that allows scientist to fine tune genetic alterations in mice; most human genes have a related mouse version; and the relatively low cost of maintaining colonies due to the rapid reproduction and short normal life span of mice [2].

The overall goal of this work is to design a small-animal positron emission tomography (PET) system specifically for imaging mice. Our two main performance metrics were to achieve <1 mm isotropic image resolution and greater than 3% absolute coincidence detection efficiency for the final system. These combined metrics for resolution and sensitivity have not yet been achieved by a small-animal PET imaging system [3,4]. Resolution is important as a 1-mm resolution in a mice-imaging system can be compared to 15 mm in a clinical system [5]. Sensitivity, however, is also important. The volume of the radiolabeled compound is limited by both the small blood volume of the mouse and the requirement that the injectant not have a pharmacologic effect. The small allowable amount of tracer limits the counting statistics of the data and, in consequence, affects statistical noise in the reconstructed image. To achieve high sensitivity, fully 3-D geometry without septa [6,7] has been adopted for many small-animal and human PET systems [6,8,9].

In this article, we report on the performance of a single detector ring scanner, referred to as QuickPET II. We previously reported on a field programmable gate array (FPGA) based electronics architecture for a partial ring (i.e., 6 detector module) scanner implementation called QuickPET I [10]. QuickPET II was constructed for evaluation of the spatial resolution imaging characteristics of our micro crystal element (MiCE) detector modules. It has a 5.76-cm in-plane field of view (FOV) and a 1.98-cm axial FOV. Due to its limited axial extent, the absolute sensitivity of the system is less than the desired 3%. In addition, whole-body mouse imaging is limited to static imaging protocols using fluorine-18 labeled radiotracers. A four-ring version of the scanner, referred to as the micro crystal element scanner (MiCES), is under construction [5,11,12] (72 total, 18 modules per ring). MiCES is being designed to meet or exceed the initial system performance requirements and to support whole-body mouse, dynamic imaging protocols. The additional detector rings will lengthen the axial FOV to ~9.5 cm. To maximize the system sensitivity, it will also employ a fully 3-D scanner geometry. Although

---

Abbreviations: CFD, constant fraction discriminator; FBP, filtered backprojection; FDG, F-18-2-fluoro-2-deoxyglucose; FORE, Fourier rebinning; FOV, field of view; MiCE, micro crystal element; MiCES, micro crystal element scanner; OSEM(DB), ordered subset expectation maximization incorporated with detector blurring.

Corresponding author: Robert S. Miyaoka, PhD, University of Washington Medical Center, Box 356004, 1959 NE Pacific Street, Seattle, WA 98195-6004; e-mail: rmiyaoka@u.washington.edu.

Received 19 August 2004; Received in revised form 21 December 2004;
Accepted 22 December 2004.

QuickPET II will eventually be replaced by MiCES, our phased development approach has proven to be very useful. QuickPET II has been a valuable developmental system to learn about the challenges involved to achieve a reconstructed image resolution of less than 1 mm^3. It has also allowed new biologic investigators unfamiliar with imaging to learn about PET through pilot imaging studies. QuickPET II system image resolution results and images from initial mouse imaging studies are presented.

Materials and Methods

MiCE Detector Modules

We have previously reported on the development of different MiCE detector designs [5,11]. The MiCE detectors used in QuickPET II consist of a 22 × 22 array of polished 0.8 × 0.8 × 10 mm mixed lutetium silicate crystals. The crystals are placed within a grid made of a highly reflective polymer film material [13] following the technique described by Miyaoka et al. [5,11]. The grid serves three purposes: (1) it optically isolates the crystals; (2) it functions as a reflective wrap; and (3) it provides structural support for the crystal array. The center-to-center spacing of the crystals within the grid is 0.9 mm. The crystal array is directly coupled to a 6 + 6 cross-anode position-sensitive photomultiplier tube (PMT) (R8520-00-C12, Hamamatsu Photonics K.K., Japan) using Histomount (National Diagnostics, Atlanta, Georgia) glue [14]. A sample crystal array and position-sensitive PMT is pictured in Figure 1.

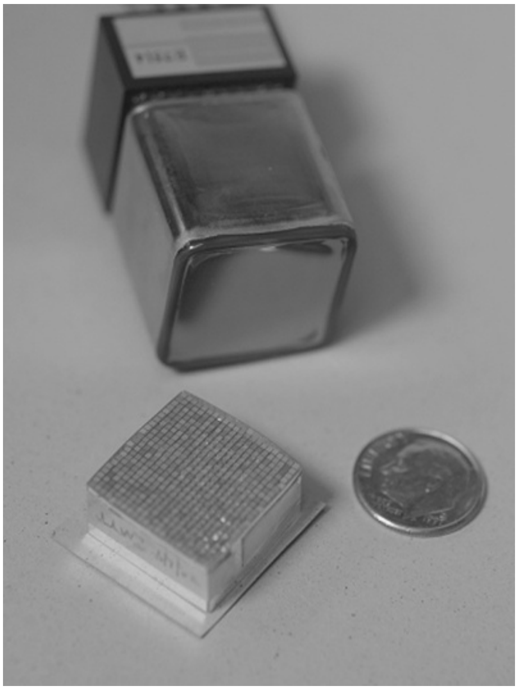

Figure 1. *Picture of MiCE crystal array and Hamamatsu position-sensitive PMT.*

An image, referred to as a crystal map (see Figures 4A and 10), illustrating the decoding performance of a MiCE detector module obtained using the techniques described by Miyaoka et al. [15] was obtained. The crystal map is a two-dimensional (i.e., x-axis and y-axis) histogram produced by mapping the ratios of the electronic signals acquired from a uniform photon flux. Each dot in the crystal map represents a crystal element. The crystal map is used to generate a look up table (LUT) that designates the crystal of interaction for a given set of position signals. The decoding characteristics of a detector module are given by the peak (i.e., the maximum value) to valley (i.e., the minimum value) ratios between neighboring crystal elements in the crystal map.

To maximize the decoding capabilities of the detector module, positioning of the crystal array on the face of the PMT is a multistep process. The initial positioning is done using a specially designed jig that positions the crystal array with respect to the external structure of the PMT. The long curing time of Histomount allows crystal maps to be collected before the glue fully sets. If the initial crystal maps indicate a slight misalignment between the crystal array and the PMT optics, the position of the crystal array is manually adjusted. This process can be repeated if necessary. Because each crystal array is individually positioned with respect to the external structure of the PMT, a crystal array alignment correction that is applied to the acquired data was developed. This procedure is described below in the subsection, "Module Alignment Correction."

A second performance characteristic of a detector module is the energy resolution of the individual crystal elements. After the crystal boundary map (i.e., the LUT) is determined, an energy histogram (i.e., energy spectrum) for each crystal element is created from the collected data. The energy resolution is determined from the energy histogram. Sample energy spectra are illustrated in Figure 4C. The peak in the energy spectrum corresponds to 511 keV photons that are photoelectrically absorbed by the detector array and is referred to as the photopeak. The energy resolution of a detector is described by the full width at half maximum (FWHM) of the photopeak divided by the bin value corresponding to the highest point of the photopeak. The lower energy events seen in the energy spectrum correspond to Compton scattered photons. The energy resolution of the crystals can affect the choice of the lower energy threshold for the detector system. However, for a scintillator-based PET imaging system optimized to image mice this generally is not the case.

QuickPET II System Electronics and Gantry

A block diagram of the QuickPET II system is shown in Figure 2. The system is made up of 18 detector modules. The detector ring is divided into three zones. Coincidences are only allowed between modules in different zones. Each module has its own "front–end" electronics card that produces four position signals (X+, X−, Y+, Y−) and a summed signal. The four position signals are used to determine which crystal within the 22 × 22 array detected the annihilation photon associated with the injected radiotracer. The summed signals are individually fed to constant fraction discriminators (CFDs): one CAEN N843, 16 channel CFD, and two TENNELEC TC453 single-channel CFDs. The CFDs produce trigger signals that are fed to a coincidence processor and an analog multiplexer board, which was developed in-house. The coincidence processor unit sends control signals (i.e., module identifier information) to the analog multiplexers informing them which set of signals to pass on. The control signals are also routed to digital-to-analog converters (DACs) that produce analog detector module identifier signals, which in turn are collected by the acquisition electronics. The acquisition electronics consists mainly of nuclear instrumentation modules and computer automated measurement and control (CAMAC) modules and has been fully described in Ref. [16].

The QuickPET II detectors, gantry and imaging table are pictured in Figure 3. The detector system consists of 18 detector modules. It has an inner ring diameter of 12.8 cm. The in-plane FOV is 5.76 cm and the axial FOV is 1.98 cm. The detector ring is mounted on a bearing that allows partial rotation of the detectors (±~20°). The purpose of adding a partial rotation was to facilitate sampling the lines of response associated with the gaps between modules. To minimize the number of rotations required per scan, the length of the animal is scanned with the detectors in one position; the detectors are rotated 10° (one half the step between modules); and the animal is scanned in the reverse direction. Due to limitations in the acquisition electronics, the rotation angle of the gantry is not monitored during data acquisition. Therefore, the detectors are not rotated during data acquisition. The imaging table (Summit Medical Equipment, Oregon) was incorporated in such a manner as to allow delivery and exhaust of gas anesthesia from a single end of the table. The tube labeled in Figure 3 is for gas delivery while channels in the table allow the exhaust to be collected from the black tube at the end of the table. Three linear stages and one vertical stage allow for accurate table placement. The table has a linear travel range of ~9 cm, enough for whole-body scanning of a mouse. For whole-body imaging studies, the table is translated, under computer control, in 1.44 cm axial FOV steps. A slight overlap of adjacent axial FOVs is required because of the fully 3-D acquisition geometry.

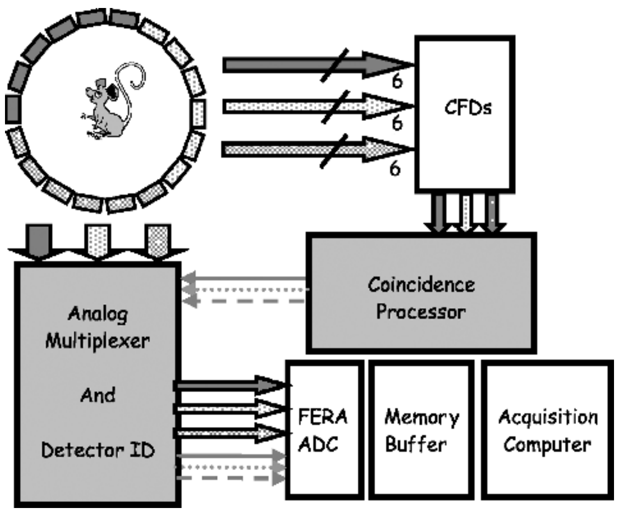

Figure 2. *Block diagram of data and control signal flow for the single ring evaluation system (QuickPET II).*

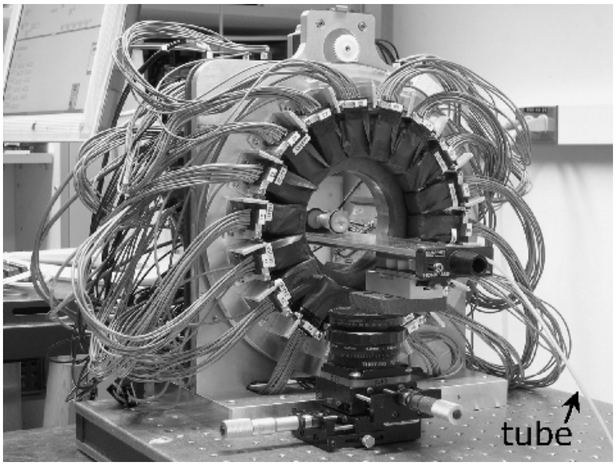

Figure 3. *Photograph of QuickPET II evaluation system, including animal imaging table.*

MiCE Detector Module Intrinsic Spatial Resolution

The intrinsic spatial resolution of a pair of MiCE detector modules was measured by stepping a line source through the axial imaging FOV of the system. The line source was a very small diameter glass capillary tube, outer diameter 0.30 mm and inner diameter unknown, filled with ^{18}F. The length of the line source was 3.25 cm and it had a slight bow to it. For protection the line source was placed within a 22-gauge needle (outer diameter 0.711 mm; inner diameter 0.394 mm) and then mounted to the edge of the system's imaging table. The height of the table was adjusted so the line source was approximately centered between two opposing detectors. From a point just outside the system's axial imaging FOV, the line source was stepped in 0.1-mm increments across the system's imaging FOV. Profile plots of the coincidence counts for each of the 22 direct slices (opposing rows of crystals) were created. A Gaussian was fit to each of the plots to determine the FWHM for each of the 22 direct slices. Ideally, a point source would be used for this measurement; however, in order to get enough activity to do the measurement, a line source was required. Any misalignment between the line source and the crystal arrays will lead to a broadening of the FWHM of the measurement.

Module Alignment Correction

A procedure was developed to estimate the crystal array offsets before binning the data [17]. The offsets were estimated by comparing simulations and measurements of two axially oriented line sources located 0 and 14 mm radially from the center of the FOV. The 18 detector modules were considered as 9 pairs of opposing detectors. For each pair of detectors, the measured data were compared to the simulated data that represents truth. The detector modules were translated in 0.225-mm steps on a 5 × 5 grid and the position resulting in the minimum root-mean-square-error (RMSE) between the measured and simulated data was determined. The transverse offsets corresponding to the minimum RMSE were chosen as the locations of the detector blocks. The corrections do not account for rotational and z-axis offsets (i.e., detector ring diameter).

Line Phantom Images

Line source measurements were made using 0.3 mm inner diameter and 0.77 mm outer diameter glass capillary tubes. Two tubes were each filled with ~16 μCi (~592 KBq) of ^{18}F. The tubes were placed parallel to one another and 14 mm apart on a thin, stiff board. Two tubes were imaged simultaneously to halve the time required for data acquisition. A tube separation of 14 mm was used so that the tails of the reconstructed line sources would not interfere with each other.

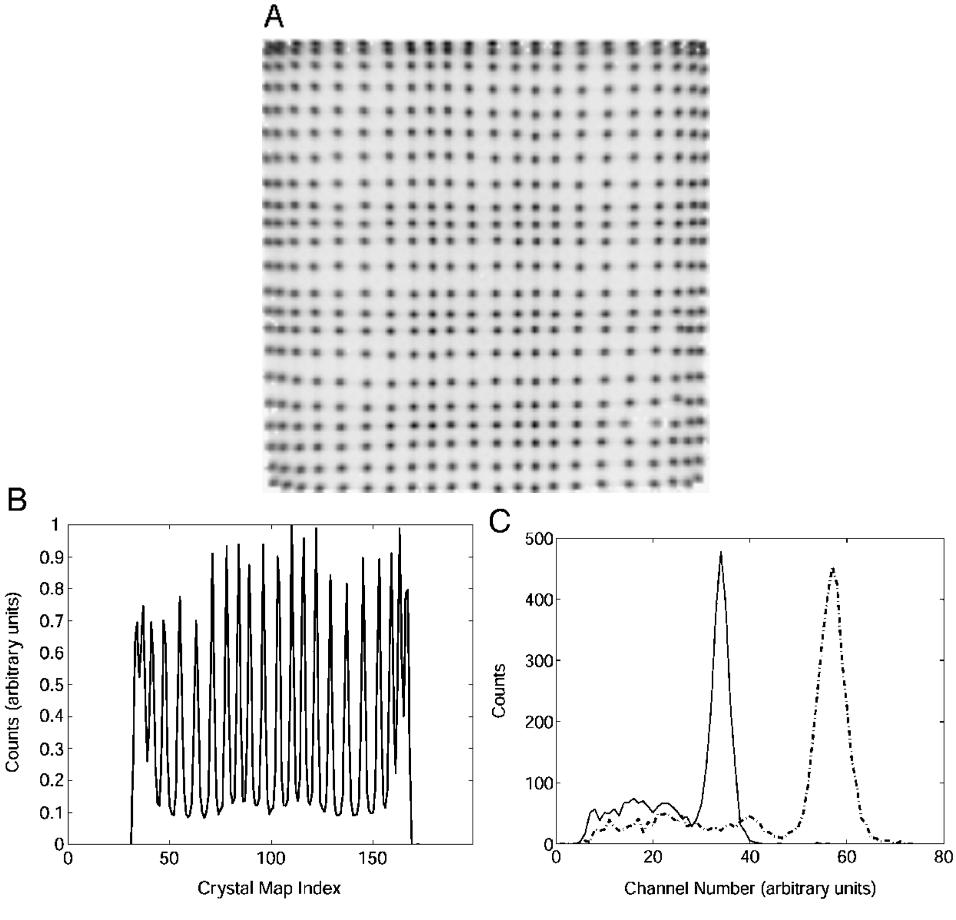

Figure 4. *(A) An image, referred to as a crystal map, illustrating the decoding characteristics for a sample MiCE detector module. Each dot in the image represents a crystal element. (B) A profile of (A) through the center row helps to further elucidate the decoding performance of a detector module. The average peak to valley ratio is ~7. (C) Sample energy spectra from individual MiCE crystals. The average energy resolution for a detector module is ~22%.*

The capillary tubes were initially positioned at 0 mm (Tube 1) and 14 mm (Tube 2) radial distance from FOV center, respectively. The tubes were stepped outward in 2-mm increments until Tube 1 overlapped the initial position of Tube 2. A total 600,000 events (2000 counts/sec × 5 min) were scanned at each source position. The data were collected in listmode (i.e., event by event) format, which includes information on each event such as the detector coordinates and the energy values of the detected photons.

The detector ring was then rotated 10° counterclockwise. Data were collected as the capillary tubes were stepped back toward the center of the detector ring. By rotating the detector ring, lines of response associated with the gaps between adjacent detector modules were sampled. All scan times were adjusted to a decay corrected length corresponding to the initial acquisition.

Mouse Studies

A C3-1 TAg [18] mouse (weight, 35 g) that spontaneously develops mammary tumors was imaged twice using F-18-2-fluoro-2-deoxyglucose (FDG). The first time it was imaged, the mouse was injected via the tail vein with 340 μCi (12.58 MBq) of FDG and placed back into its cage during the uptake phase of the FDG. Imaging for the mouse began 3 hr 40 min after injection. The long delay between injection and imaging was due to two factors: (1) to let the activity decay to a level more optimal for the QuickPET II scanner and (2) a second mouse was imaged. The mouse was imaged again 10 days later. For the second study, the mouse was injected with 200 μCi (7.4 MBq) FDG via the tail vein. After injection, it was kept in the induction box under a low level of anesthesia (~0.5% isoflurane) for 50 min before imaging began. Four axial FOV scans were acquired for both imaging procedures.

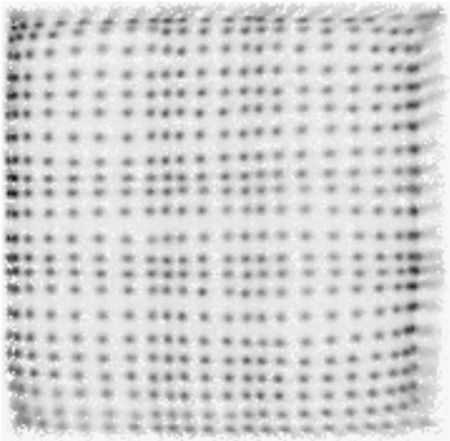

Figure 5. *An example of a crystal map with poor decoding of crystal elements along the right edge of the map.*

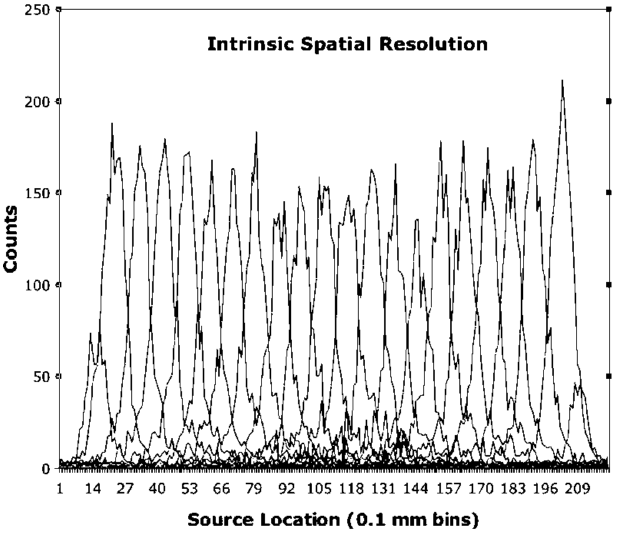

Figure 6. *Intrinsic spatial resolution of the system measured with an ^{18}F line source less than 0.4 mm in diameter. Average FWHM is 1.05 mm for the 22 direct slices without correction for the source size. FWHM values were determined from a Gaussian fit to the measured data.*

A p53 heterozygote female mouse (weight, 30 g) on an NIH background [19] with chemically induced skin tumors was imaged with FDG. The mouse was injected with 240 μCi (8.88 MBq) of FDG via tail vein injection. Imaging began approximately 1 hr postinjection. To reduce uptake in the background tissues, the mouse was kept under light anesthesia (0.5–2.0% isoflurane) during radiopharmaceutical uptake. A 5 axial FOV scan was acquired over ~90 min; 21.3 million events were acquired during the study. Due to a handling error, the mouse was fed just before imaging and there was intense cardiac uptake as well as the expected tumor uptake.

Image Reconstruction

Fully 3-D sinogram data were rebinned into a stacked set of contiguous 2-D sinograms using either the single slice rebinning [20] or Fourier rebinning (FORE) [21] algorithms. The rebinning process accelerates the image reconstruction process by reducing the fully 3-D ray-tracing problem to a stack of much faster 2-D ray-tracings. The module alignment corrections were applied before rebinning of the data. After rebinning, data were corrected for sampling density. No other corrections (e.g., attenuation, scatter, randoms, or other normalization corrections) are currently being applied. Reconstruction algorithm options include 2-D versions of filtered-backprojection (FBP) [22] and ordered-subsets expectation-maximization (OSEM) [23,24] using the ASPIRE library [25]. In addition, we have also developed an iterative reconstruction utilizing a factorized system model including detector blurring (DB). This method is referred to as OSEM(DB) [17]. The FBP images were reconstructed with a Hamming filter at the Nyquist frequency (i.e., 0.9 mm FWHM). A 0.9-mm Gaussian filter was applied to the OSEM images. No postfiltering was applied to the OSEM(DB) images. For both OSEM reconstructions, eight iterations and eight subsets were used.

Results

MiCE Detector Modules

A detector crystal map image is illustrated in Figure 4A. In one dimension, the peak and valley values are best visualized by looking at a profile through a row of crystals in the crystal map, as shown in Figure 4B. The average peak-to-valley ratio for our detector modules was ~7. Sample energy spectra from both a crystal with good light collection efficiency and low light collection efficiency are shown in Figure 4C. The average energy resolution for the individual crystals was ~22% (<20% if edge crystals are not included).

The production MiCE detectors used for QuickPET II have slightly degraded decoding performance along the edges of the crystal arrays compared to the initial prototype detectors [10]. An example of a detector with poor decoding along one of its edges is illustrated in Figure 5. The dark dots on the right side of the crystal map correspond to two crystals. The gray tails along the edge of the crystal map correspond to low energy events and are generally not included in the individual crystal look up tables (i.e., they are excluded once energy thresholds are applied on a crystal by crystal basis). The main reason for the slightly degraded performance is that the center-to-center crystal spacing was increased from 0.88 mm for the prototype crystal arrays to 0.90 mm for the production crystal arrays. This 0.02-mm increase in the crystal spacing translates into a 0.42-mm increase in the linear size of the crystal

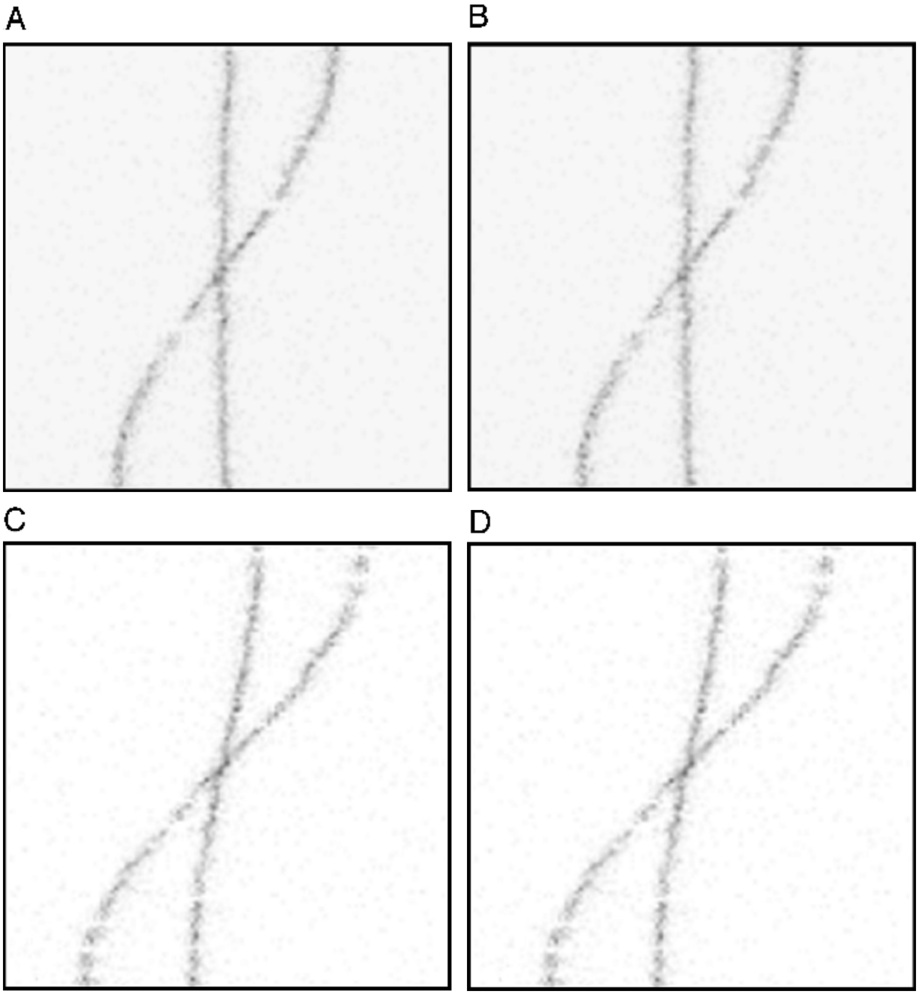

Figure 7. *(A) Sinogram of line sources at center and offset by 14 mm without alignment correction. (B) Sinogram of line sources at center and offset by 14 mm with alignment correction. (C) Sinogram of line sources offset by 4 and 18 mm. (D) Sinogram of line sources offset by 8 and 22 mm. All sinograms were rebinned using single slice rebinning and ±3 slices.*

array that leads to decreased light collection efficiency for the edge crystals. To improve the decoding for crystals along the edge of the PMT, we are redesigning the front–end amplifier board to include threshold amplifiers. The use of threshold amplifiers has been shown to improve the edge decoding performance for detectors using Anger style positioning [26]. Additional reasons for the slightly degraded performance are that many of the current crystal arrays have been glued and unglued multiple times as the fabrication technique was being optimized and the use of analog multiplexers in the data acquisition electronics.

MiCE Detector Module Intrinsic Spatial Resolution

The FWHM for the 22 direct slices of the detector module ranged from 0.99 to 1.15 mm, with a mean of 1.05 ± 0.07 mm, without correction for the line source (see Figure 6). The FWHM values were calculated from Gaussian fits to the measured data. The differences in the peak heights of the edge rows of crystals are caused by poor decoding of the edge crystals and the lower sensitivity of the edge crystals. The results were measured with the detectors in the gantry and the signals processed using all of the QuickPET II data acquisition electronics. Again, any rotational misalignments between the line source and the detector modules or the detector modules themselves will lead to a broadening of the measured intrinsic spatial resolution. Still these results are slightly better than the 1.21 mm average FWHM reported by Tai et al. [3] for the MicroPET II detectors measured in the system using a 0.5-mm diameter ^{22}Na point source and equal to the 1.05-mm FWHM reported by Chatziioannou et al [27] for a pair of prototype detectors and a 0.33-mm diameter ^{18}F needle source.

Line Phantom Images

Sinograms of the multiline source phantom are illustrated in Figure 7. The data were binned using single

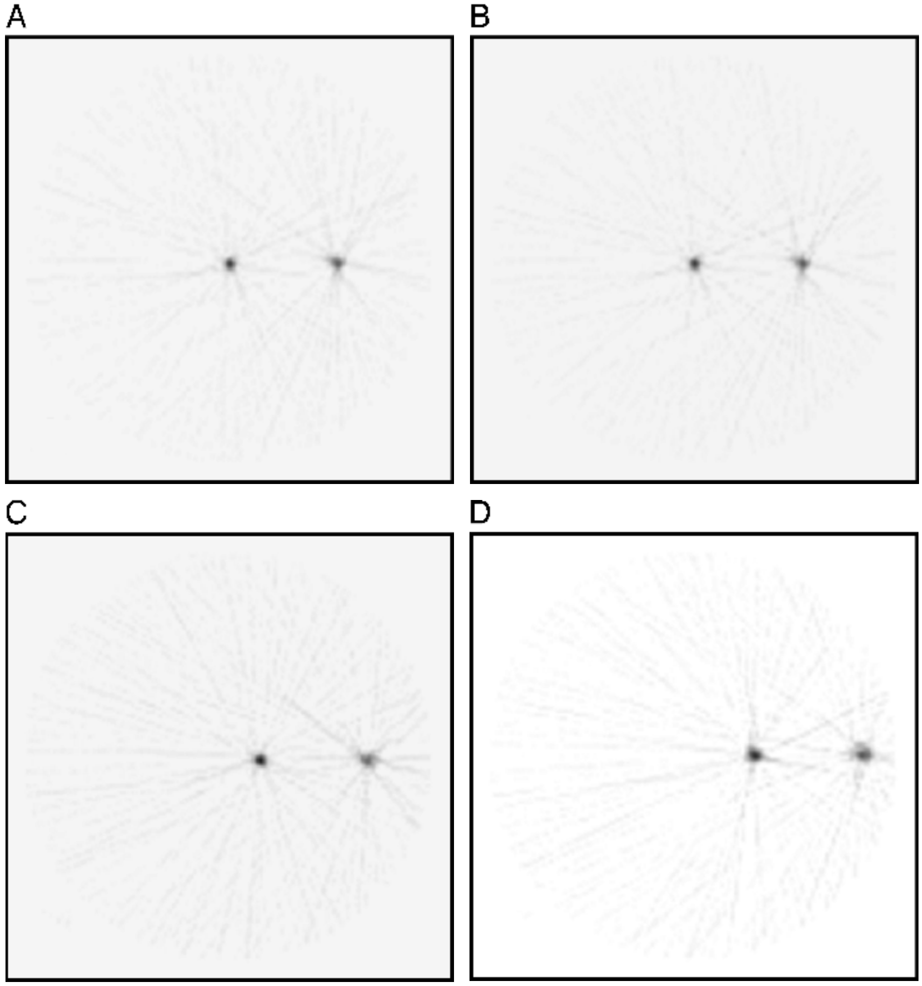

Figure 8. *(A) Reconstructed image of line sources at center and with a transverse offset of 14 mm without alignment correction. (B) Reconstructed image of line sources at center and offset by 14 mm with alignment correction. (C) Reconstructed image of line sources offset by 4 and 18 mm. (D) Reconstructed image of line sources offset by 8 and 22 mm. All images reconstructed with FBP and a ramp filter at Nyquist frequency.*

Table 1. Line Source Image Resolution

Position of Line Source	Radial Profiles[a] FWHM (mm)	Radial Profiles[a] FWTM (mm)	Tangential Profiles[a] FWHM (mm)	Tangential Profiles[a] FWTM (mm)
0 mm (no correction)	1.3 ± 0.05	3.0 ± 0.26	1.5 ± 0.38	2.9 ± 0.99
14 mm (no correction)	1.6 ± 0.05	4.1 ± 0.07	1.8 ± 0.36	4.5 ± 0.84
0 mm (with correction)	1.2 ± 0.06	3.0 ± 0.39	1.2 ± 0.05	2.9 ± 0.29
4 mm (with correction)	1.3 ± 0.05	2.9 ± 0.30	1.2 ± 0.04	2.7 ± 0.18
8 mm (with correction)	1.5 ± 0.09	3.8 ± 0.60	1.3 ± 0.08	3.7 ± 0.52
14 mm (with correction)	1.5 ± 0.10	3.8 ± 0.53	1.5 ± 0.16	4.4 ± 0.40
18 mm (with correction)	2.2 ± 0.13	4.7 ± 0.64	1.5 ± 0.12	4.8 ± 0.54
22 mm (with correction)	2.2 ± 0.11	5.0 ± 0.39	1.5 ± 0.16	5.2 ± 0.44

[a] No correction for the size of line source was included.

slice rebinning with three plane differences. The sinograms include data with the gantry rotated to sample the gaps between the detectors. Figure 7A is a sinogram, without any alignment adjustment, for the line sources centered and at a 14-mm radial offset. Figure 7B–D contains sinograms after application of our detector alignment adjustment technique. The data were reconstructed using FBP and a ramp filter at Nyquist frequency. The reconstructed images are illustrated in Figure 8. The average FWHM and the average full width at tenth maximum (FWTM) values for the different line source positions are listed in Table 1. The values listed are for all 22 direct imaging planes and are not adjusted for the size of the source. Applying our current alignment correction led to a slight improvement in our image resolution. Methods to estimate residual misalignments for each of the 6 degrees of freedom associated with the location and orientation of each detector module are under development. We believe this is a critical component to fully realize the intrinsic spatial resolution characteristics of our MiCE detectors.

Mouse Studies

The images of the C3-1 TAg mouse in Figure 9 illustrate how sedation of the mouse improves the uptake of FDG in tumors. These results are consistent with other FDG tumor imaging protocols we have conducted on tumor bearing mice and not due to difference in the uptake period for the two studies. In fact for human FDG imaging, lengthening the uptake period usually improves the tumor-to-background contrast [28]. Both datasets were binned using single slice rebinning with nine ring differences and reconstructed using FBP with a Hamming filter at 0.8 the Nyquist frequency (1.13 mm FWHM).

The intense uptake in the heart of the mouse bearing the skin tumors provided an ideal dataset to examine differences between FBP, OSEM, and our OSEM(DB)

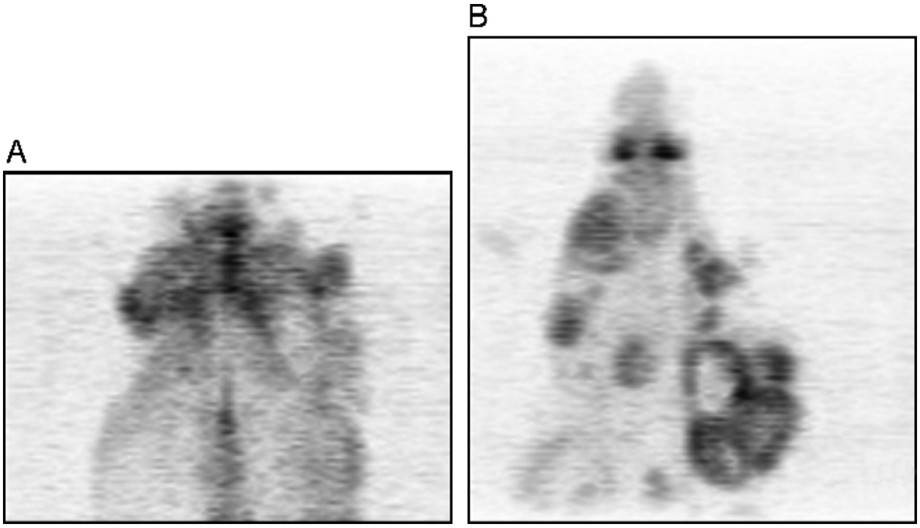

Figure 9. *(A) C3-1 TAg mouse imaged with FDG with no anesthesia during uptake phase. (B) Same mouse imaged 10 days later. For the second scan the mouse was under anesthesia during uptake phase of FDG.*

image reconstructions. Mouse heart images were reconstructed with each of the three different reconstruction techniques (after FORE rebinning). Transaxial and coronal slices through the heart (non-reoriented) are illustrated in Figure 10. The images reconstructed using OSEM are slightly sharper than the FBP images. The OSEM(DB) images were significantly sharper due to the resolution recovery associated with modeling the 2-D detector response function within the system matrix. Hot spots are visible in each of the image sets. Because they appear in the FBP images, we believe they are either a normalization artifact or physiologic uptake

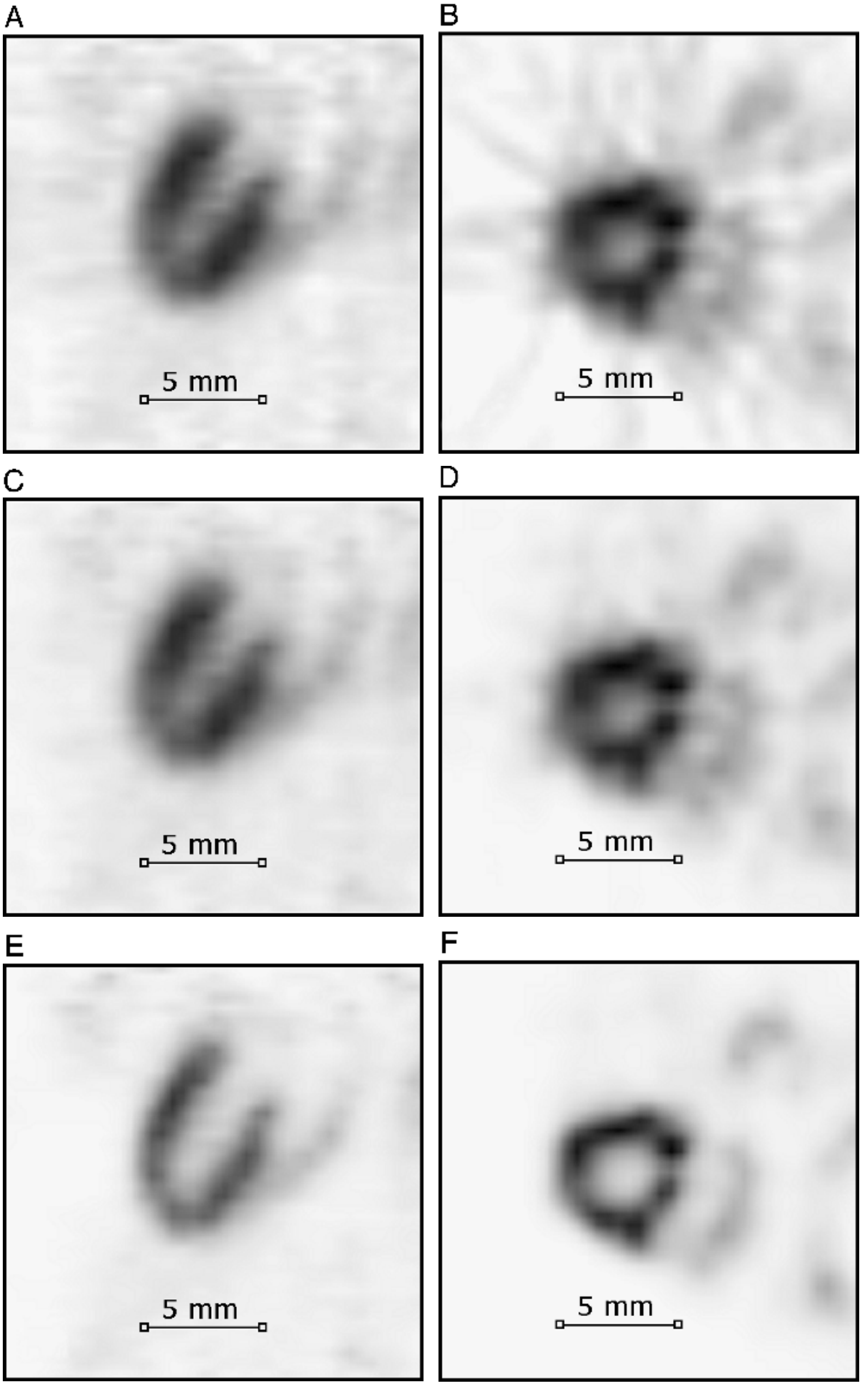

Figure 10. *Heart images of p53 heterozygote mouse. FORE + FBP, 0.9 mm Hamming filter: (A) Coronal slice; (B) Transaxial slice. FORE + OSEM, 0.9 mm Gaussian postfilter: (C) Coronal slice; (D) Transaxial slice. FORE + OSEM(DB): (E) Coronal slice; (F) Transaxial slice.*

differences in the heart rather than an artifact caused by the iterative reconstruction methods. Figure 11 shows a maximum intensity pixel display through the whole-body mouse image volume reconstructed by the FORE + OSEM(DB) approach. FDG uptake of skin tumors are well recognized with improved resolution by the FORE + OSEM(DB).

Conclusions

The main limitation of the QuickPET II single detector ring system is the low count rate capability of the data acquisition system. To overcome this limitation, a high bandwidth data acquisition system using the IEEE 1394a SBP-2 protocol is under development for the full MiCES system [12].

The measured image resolution using FBP is approaching our goal for isotropic <1 mm FWHM, and improved detector alignment correction algorithms will achieve this goal.

Results from the mouse studies demonstrate the high-resolution imaging potential of the MiCES PET system for in vivo imaging. Keeping the mouse sedated during the uptake phase for FDG imaging is important. How gas anesthesia (e.g., isoflurane) affects the physiologic state of the animal needs further exploration.

The mouse heart images demonstrate the potential for using accurate modeling of the imaging system to improve image resolution for very high resolution imaging systems.

In conclusion, a single ring version of our MiCES small-animal PET system is operational and has been used for static PET imaging of mice using ^{18}F labeled radiotracers. The image resolution for the system has been measured at 1.2 mm FWHM using FBP with a ramp filter for a line source centered in the FOV of the system. We expect improvements in the resolution as new front–end detector electronics and better mechanical misalignment corrections are implemented. Methods to estimate residual misalignments for each of the 6 degrees of freedom associated with the location and orientation of each detector module are under development. Image reconstruction methods that include models of the physical effects associated with high-resolution scanning have significant potential to improve the reconstructed spatial resolution. With the QuickPET II evaluation system, structures such as the right ventricle of the heart are already visible using FDG.

Figure 11. *Maximum intensity pixel projection image of p53 heterozygote mouse reconstructed by FORE + OSEM(DB). The same mouse data as Figure 10 was used for the reconstruction.*

Acknowledgments

This work was supported by in part by PHS grants CA88194, CA74135, EB002117, and U01ES10045. The authors thank Drs. Ken Krohn, Steve Shoner, and John Grierson for providing us with FDG for the system calibration and mouse imaging studies. The authors would also like to acknowledge the laboratories of Drs. Warren Ladiges and Chris Kemp whose mice were used in the imaging studies.

References

[1] Chatziioannou AF (2002). Molecular imaging of small animals with dedicated PET tomographs. *Eur J Nucl Med.* **29**:98–114.

[2] Weissleder R, Mahmood U (2001). Molecular imaging. *Radiology.* **219**:316–333.

[3] Tai YC, Chatziioannou AF, Yang YF, Silverman RW, Meadors K, Siegel S, Newport DF, Stickel JR, Cherry SR (2003). MicroPET II: Design, development and initial performance of an improved MicroPET scanner for small-animal imaging. *Phys Med Biol.* **48**:1519–1537.

[4] Jeavons AP, Chandler RA, Dettmar CAR (1999). A 3D HIDAC-PET camera with sub-millimetre resolution for imaging small animals. *IEEE Trans Nucl Sci.* **46**:468–473.

[5] Miyaoka RS, Kohlmyer SG, Lewellen TK (2001). Performance characteristics of micro crystal element (MiCE) detectors. *IEEE Trans Nucl Sci.* **48**:1403–1407.

[6] Cherry SR, Shao Y, Silverman RW, Meadors K, Siegel S, Chatziioannou AF, Young JW, Jones WF, Moyers JC, Newport D, Boutefnouchet A, Farquhar TH, Andreaco M, Paulus MJ, Binkley DM, Nutt R (1997). Phelps ME, MicroPET: A high resolution PET scanner for imaging small animals. *IEEE Trans Nucl Sci.* **44**:1161–1166.

[7] Bendriem B, Townsend DW (1998). *The theory and practice of 3D PET.* Dordrecht, The Netherlands: Kluwer Academic Publishing.

[8] Lecomte R, Cadorette J, Rodrigue S, Rouleau D (1994). Design

and engineering aspects of a high resolution positron tomograph for small animal imaging. *IEEE Trans Nucl Sci.* **41**:1446–1452.

[9] Cherry SR, Dahlbom M, Hoffman EJ (1991). 3D PET using a conventional multislice tomograph without septa. *JCAT.* **15**: 655–668.

[10] Laymon CM, Miyaoka RS, Park BK, Lewellen TK (2003). Simplified FPGA-based data acquisition system for PET. *IEEE Trans Nucl Sci.* **50**:1483–1486.

[11] Miyaoka RS, Kohlmyer SG, Joung J, Lewellen TK (2001). Performance characteristics of a second generation micro crystal element (MiCE2) detector. *IEEE Nucl Sci Symp Med Imaging Conf Rec.* **2**:1124–1127.

[12] Lewellen TK, Laymon Miyaoka RS, Janes ML, Park BK, Gillispie SG, Lee K, Kinahan PE (2003). System electronics for the MiCES small animal PET scanner. *2003 IEEE Nuclear Science Symposium and Medical Imaging Conference.* Conference record on CD. Portland, Oregon.

[13] Weber MF, Stover CA, Gilbert LR, Nevitt TJ, Ouderkirk AJ (2000). Giant birefringent optics in multilayer polymer mirrors. *Science.* **287**:2451–2456.

[14] Montecchi M, Ingram Q (1995). Study of some optical glues for the compact muon solenoid at the large hadron collider of CERN. *NIM Phys Res A.* **465**:329–345.

[15] Miyaoka RS, Janes ML, Lewellen, TK (2003). Optimization of mounting large crystal arrays to photomultiplier tubes. *IEEE Nuclear Science Symposium and Medical Imaging Conference.* Conference record in CD. Portland, Oregon.

[16] Lewellen TK, Miyaoka RS, Jansen F, Kaplan MS (1997). A data acquisition system for coincidence imaging using a conventional dual head gamma camera. *IEEE Trans Nucl Sci.* **44**:1214–1218.

[17] Lee K, Kinahan PE, Fessler JA, Miyaoka RS, Janes M, Lewellen TK (2004). Pragmatic image reconstruction for the MiCES fully-3D mouse imaging PET scanner. *Phys Med Biol.* **49**:4563–4578.

[18] Green JE, Shibata MA, et al. (2000). The C3(1)/SV40 T-antigen transgenic mouse model of mammary cancer: Ductal epithelial cell targeting with multistage progression to carcinoma. *Oncogene.* **19**:1020–1027.

[19] Kemp CJ, Donehower LA, Bradley A, Balmain A (1993). Reduction of p53 gene dosage does not increase initiation or promotion but enhances malignant progression of chemically induced skin tumors. *Cell.* **74**:813–822.

[20] Daube-Witherspoon ME, Muehllehner G (1987). Treatment of axial data in three dimensional PET. *J Nucl Med.* **28**:1717–1724.

[21] Defrise M, Kinahan PE, Townsend DW, Michel C, Sibomana M, Newport DF (1997). Exact and approximate rebinning algorithms for 3-D PET data. *IEEE Trans Med Imag.* **16**:145–158.

[22] Kak AC, Slaney M (1988). *Principles of computerized tomographic imaging*. New York, New York: IEEE Press.

[23] Hudson HM, Larkin RS (1994). Accelerated image reconstruction using ordered subsets of projection data. *IEEE Trans Med Imag.* **13**:601–609.

[24] Comtat C, Kinahan PE, Defrise M, Michel C, Townsend DW (1998). Fast reconstruction of 3D PET data with accurate statistical modeling. *IEEE Trans Nucl Sci.* **45**:1083–1089.

[25] Fessler JA (2001). Aspire 3.0 user's guide: A sparse iterative reconstruction library. Technical report no. 293. Communications and Signal Processing Laboratory. University of Michigan.

[26] Wojcik R, Majewski S, Kross B, Popov V, Weisenberger AG (2001). Optimized readout of small gamma cameras for high resolution single gamma and positron emission imaging. *IEEE Nuclear Science Symposium and Medical Imaging Conference* (pp. 1821–1825). San Diego, California.

[27] Chatziioannou A, Tai YC, Doshi N, Cherry SR (2001). Detector development for microPET II: A 1 μl resolution PET scanner for small animal imaging. *Phys Med Biol.* **46**:2899–2910.

[28] Spence AM, Muzi M, Mankoff DA, O'Sullivan SF, Link JM, Lewellen TK, Lewellen B, Pham P, Minoshima S, Swanson K, Krohn K (2004). ^{18}F-FDG PET of gliomas at delayed intervals: Improved distinction between tumor and normal gray matter. *J Nucl Med.* **45**:1653–1659.